

Magnetic field generation and amplification in an expanding plasma

K. M. Schoeffler,¹ N. F. Loureiro,¹ R. A. Fonseca,^{1,2} and L. O. Silva¹

¹*Instituto de Plasmas e Fusão Nuclear — Laboratório Associado,
Instituto Superior Técnico, Universidade de Lisboa, 1049-001 Lisboa, Portugal*

²*DCTI/ISCTE Instituto Universitário de Lisboa, 1649-026 Lisboa, Portugal*
(Dated: November 21, 2019)

Particle-in-cell simulations are used to investigate the formation of magnetic fields, \mathbf{B} , in plasmas with perpendicular electron density and temperature gradients. For system sizes, L , comparable to the ion skin depth, d_i , it is shown that $B \sim d_i/L$, consistent with the Biermann battery effect. However, for large L/d_i , it is found that the Weibel instability (due to electron temperature anisotropy) supersedes the Biermann battery as the main producer of B . The Weibel-produced fields saturate at a finite amplitude (plasma $\beta \approx 100$), independent of L . The magnetic energy spectra below the electron Larmor radius scale is well fitted by power law with slope $-16/3$, as predicted in Schekochihin *et al.*, *Astrophys. J. Suppl. Ser* **182**, 310 (2009).

PACS numbers: 52.35.Qz, 52.38.Fz, 52.65.Rr, 98.62.En

Introduction. The origin and amplification of magnetic fields is a central problem in astrophysics [1]. The turbulent dynamo [2, 3] is generally thought to be the basic process behind the amplification of a magnetic seed field; however, some other process is required to originate the seed itself. Amongst the few mechanisms able to do so is the Biermann battery effect, due to perpendicular electron density and temperature gradients [4]. It is often conjectured that the observed magnetic fields in the universe may be of Biermann origin, subsequently amplified via dynamo action [1]. However, simple theoretical estimates suggest that Biermann-generated magnetic fields, \mathbf{B} , should be such that [5–7]

$$\beta \equiv 8\pi P/B^2 \sim (d_i/L)^{-2}, \quad (1)$$

where P is the plasma pressure, $d_i = c/\omega_{pi}$ is the ion inertial length (with c the speed of light and ω_{pi} the ion plasma frequency) and L is the characteristic length scale of the system. Given the extremely small values of d_i/L typical of astrophysical systems, it is an open question whether such seeds are sufficiently large to account for the microgauss fields observed today.

Megagauss magnetic fields are observed to form in intense laser-solid interaction laboratory experiments [8–11]. In these experiments, the laser generates an expanding bubble of plasma by ionizing a foil of metal or plastic. The plasma is denser closer to the plane of the target foil, and hotter closer to the laser beam axis. Perpendicular density and temperature gradients are thus generated, giving rise to magnetic fields via the Biermann effect. Besides their intrinsic interest, these experiments offer a unique opportunity to illuminate a fascinating, and poorly understood, astrophysical process.

In this Letter we perform *ab initio* numerical investigations of the generation and growth of magnetic fields in a configuration akin to that of laser-generated plasma systems. For small to moderate values of the parameter L/d_i our simulations confirm the theoretical predic-

tions of Haines [7]; in particular, for $L/d_i \gtrsim 1$ the magnetic fields obey the scaling of Equation (1). However, when $L/d_i \gg 1$, we find that the plasma is unstable to the Weibel instability [12], which amplifies the magnetic fields such that $\beta \approx 100$, independent of L . As we will show, these results have strong implications for the interpretation of laser-solid interaction experiments; they also shed new light on the currently accepted view of the origin of the observed cosmic magnetic fields.

Computational Model. We perform a set of particle-in-cell (PIC) simulations using the OSIRIS framework [13, 14]. The initial fluid velocity, electric field, and magnetic field are all uniformly zero. We start with a spheroid distribution of density, that has a shorter length scale in one direction:

$$n = \begin{cases} (n_0 - n_b) \cos(\pi R_1/2L_T) + n_b, & \text{if } R_1 < L_T, \\ n_b, & \text{otherwise,} \end{cases} \quad (2)$$

where $R_1 = \sqrt{x^2 + y^2 + (L_T/L_n z)^2}$ and $n_b = 0.1n_0$ is the uniform background density. The characteristic lengths of the temperature and density gradients generated by the laser beam are denoted by L_T and L_n , respectively. To represent the recently ionized foil, which is flatter in the direction of the laser, z , we set $L_T/L_n = 2$ (this is a generic choice that appears to be qualitatively consistent with experiments, e.g. [9–11]; note, however, that the specific value of L_T/L_n depends on target and laser properties and thus can vary). The initial velocity distributions are Maxwellian, with a uniform ion thermal velocity v_{Ti0} . The spatial profile for the electron thermal velocity is cylindrically symmetric along the z direction, where it is hottest in the center:

$$v_{Te} = \begin{cases} (v_{Te0} - v_{Te b}) \cos(\pi R_2/2L_T) + v_{Te b}, & \text{if } R_2 < L_T, \\ v_{Te b}, & \text{otherwise,} \end{cases} \quad (3)$$

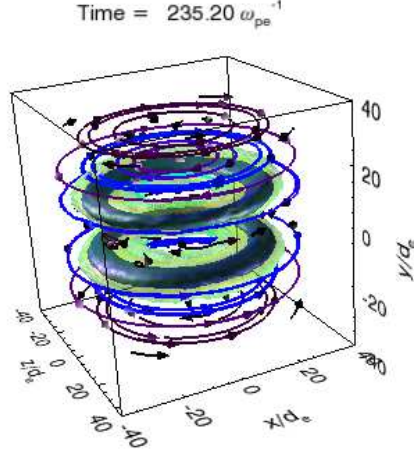


FIG. 1. Magnetic energy contours after saturation ($t\omega_{pe} = 235.2$, see Fig. 3) from a 3D simulation with $L_T/d_e = 50$. Lighter to darker colors represent $B^2/8\pi P_{e0} = 0.0035, 0.0071, 0.0106$. Several magnetic field lines are also displayed.

where $R_2 = \sqrt{x^2 + y^2}$, resulting in a maximum initial electron pressure $P_{e0} = m_e n_0 v_{Te0}^2/2$. The numerical values of the thermal velocities are $v_{Te0} = 0.2c$ and $v_{Ti0} = v_{Teb} = 0.01c$. Note that in our setup the pressure is dominated by the electrons, and thus $\beta \approx \beta_e \equiv 8\pi P_e/B^2$. For simplicity the boundaries are periodic, but the box is large enough that they do not interfere with the dynamics [$L_{(x,y,z)max} = -L_{(x,y,z)min} = 15/8 L_T$]. In order to investigate a larger range of L_T/d_i , the simulations are run with a reduced mass ratio of 25. The spatial resolution is 16 gridpoints/ d_e , or 2.26 gridpoints/ λ_d , where $d_e = c/\omega_{pe}$ is the electron inertial length (ω_{pe} is the electron plasma frequency) and λ_d is the electron Debye length. The time resolution is $\Delta t\omega_{pe} = 0.07$. The 2D simulations have 196 or 64 particles per cell (ppc); the 3D simulation has 27 ppc.

Biermann regime. Figure 1 shows contours of constant magnetic energy density and magnetic field lines from a 3D simulation with $L_T/d_e = 50$ taken at $t\omega_{pe} = 235.2$, after the magnetic field strength saturates (see timetrace in Fig. 3). As expected based on the initial conditions, we observe the formation of large scale azimuthal Biermann magnetic fields which are nearly axisymmetric. We believe this is the first ever fully self-consistent kinetic 3D simulation to show the production of magnetic fields via the Biermann effect.

The axisymmetry yielded by the 3D simulation suggests that a scaling study in system size can be performed using a more computationally efficient 2D setup instead. To this end, we take a cut of the 3D system at $z = 0$, where the azimuthal (out-of-plane) magnetic fields are in the z direction, and perform a set of 2D simulations with $L_T/d_e = (4, 8, 16, 25, 32, 50, 64, 128, 200, 400)$. For

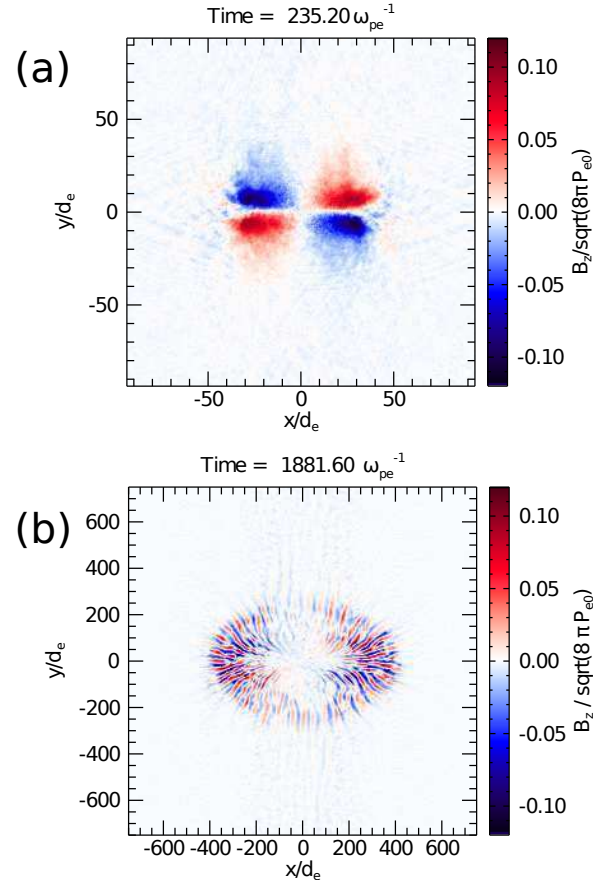


FIG. 2. Out-of-plane magnetic field, B_z , after saturation (see Fig. 3) for (a) $L_T/d_e = 50$, and (b) $L_T/d_e = 400$.

$4 \leq L_T/d_e \leq 128$ we use 196 ppc. For $L_T/d_e = 200, 400$ we use 64 ppc instead due to computing time limitations; convergence studies at lower values of L_T/d_e do not show significant differences between 196 and 64 ppc. A snapshot taken at the same time of a 2D version of the simulation presented in Fig. 1 is shown in Fig. 2(a) for comparison. The same large-scale magnetic field structure is manifest, and very similar levels of B_z are attained.

The time trace of the maximum magnetic field strength for a selection of cases can be seen in Fig. 3(a). For small systems, $L_T/d_e < 50$, the magnetic field reaches a maximum and then decays away. On the other hand, we observe that for $L_T/d_e > 50$ the magnetic field saturates at around its peak value.

Figure 3(b) shows the scaling with system size of the maximum and the average magnitude of the magnetic field (the square root of the box-averaged B_z^2) at the time when the field saturates (or peaks for $L_T/d_e < 50$). There are three distinct regions in this plot. For $L_T/d_e < 25$ (i.e., $L_T/d_i \lesssim 5$), the magnetic field increases with system size. This stage is followed by a region where the saturated amplitude of the field decreases as d_i/L_T , which lasts while $L_T/d_e < 100$. These two stages confirm the theoretical prediction of Haines [7]: in very small sys-

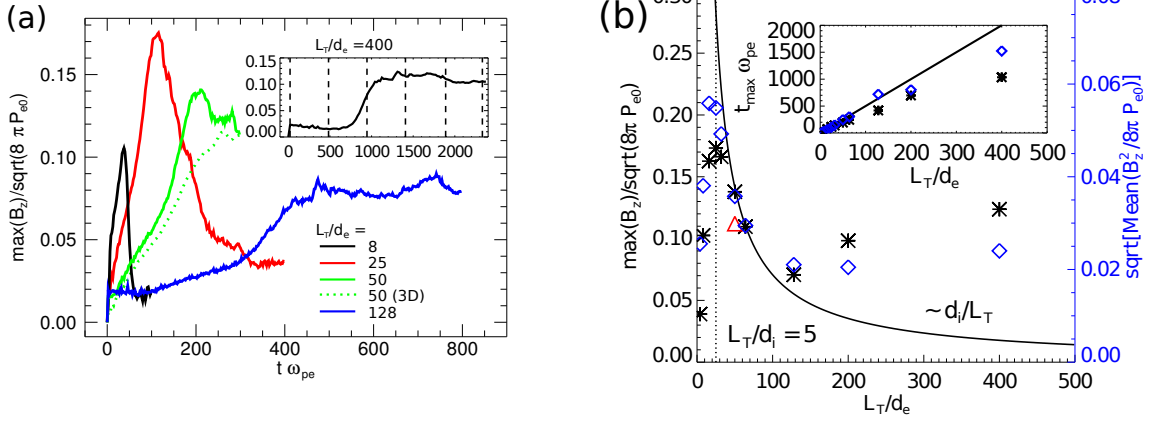


FIG. 3. (a) Maximum B_z vs. time for a selection of system sizes (L_T/d_e). The inset shows the $L_T/d_e = 400$ case. Dashed lines identify the times at which the spectra of Fig. 5 are calculated. (b) Maximum (asterisks), and average magnitude (diamonds) of B_z vs. L_T/d_e . The triangle represents the maximum B_z for the 3D run. The solid curve is $\max(B_z)/\sqrt{8\pi P_{e0}} = \sqrt{2}d_i/L_T$; the dotted line indicates $L_T/d_i = 5$. The inset shows the time to maximum magnetic field, t_{max} , vs. L_T/d_e . The solid line indicates $t_{max} = L_T/v_{Te0}$.

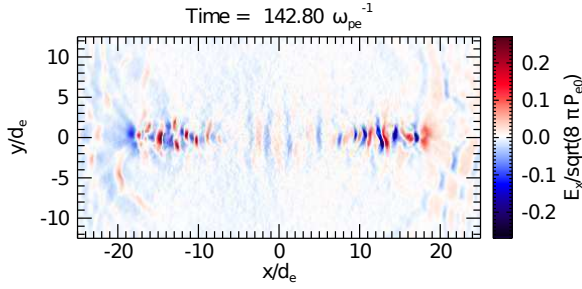


FIG. 4. Electric field in the x -direction, E_x , for $L_T/d_e = 25$ at $t\omega_{pe} = 142.8$.

tems, there is a competition between the Biermann battery effect and microinstabilities (the ion acoustic and the lower hybrid drift instabilities), triggered by an electron drift velocity in excess of the ion acoustic speed, which suppress the Biermann fields. As the system becomes larger, the electron drift velocity decreases (larger systems have larger-scale magnetic fields, and therefore lower currents). The microinstabilities thus become progressively less virulent until their complete suppression, whereupon we encounter a “pure” Biermann regime. Inspection of the simulations for $L_T/d_e < 50$ at times after the magnetic field reaches its peak value shows clear electric field perturbations along $y = 0$, consistent with the ion acoustic instability. These are exemplified for $L_T/d_e = 25$ in Fig. 4. Note that the density gradient goes to zero at $y = 0$, ruling out the lower hybrid drift instability as the cause of the decay of the magnetic field.

Weibel regime. An unexpected third regime is encountered for $L_T/d_e > 100$. In that region of Fig. 3(b), the magnetic field produced in our simulations no longer follows the predicted d_i/L_T Biermann scaling, but rather increases with the system size and appears to tend to

a constant, finite, value, $\beta_e \approx 100$. As exemplified in Fig. 2(b) for our largest simulation ($L_T/d_e = 400$), the large-scale coherent Biermann magnetic fields characteristic of the smaller systems are replaced by non-propagating magnetic structures with very short wavelengths ($\sim 5d_e$), and with a transverse wave vector, \mathbf{k} , perpendicular to the direction with a larger temperature. These features are consistent with the Weibel instability [12, 15, 16].

Indeed, the Weibel instability is expected in our system. As the initial cloud of plasma expands due to the imposed density gradient, outward ion and electron flows are generated. The velocity of these flows will vary along the temperature gradient. The higher temperature flows, originating in the center, stream past lower temperature flows originating further outward. This generates a larger velocity spread (larger temperature) in the direction of the flow, while the perpendicular temperature remains unaffected. It is this anisotropy that drives the Weibel instability. In our simulations we observe an enhanced temperature in the direction of the density gradient, consistent with this picture (not shown). In addition, along $x = 0$, where the temperature gradient is zero and thus no anisotropy is generated, the Weibel instability is not observed [see Fig. 2(b)]. Note that the Weibel instability cannot occur below a certain system size because it is suppressed by the strong, large scale Biermann fields (we have confirmed this suppression numerically by running a similar setup where the Biermann effect is not present; see also [17].)

The transition between the Biermann and Weibel regimes is also visible in the inset plot in Fig. 3(b), where we show the time to reach the maximum magnetic field, t_{max} , as a function of system size. For $L_T/d_e < 50$, we find that $t_{max} \sim L_T/v_{Te0}$. A linear in time scaling is in-

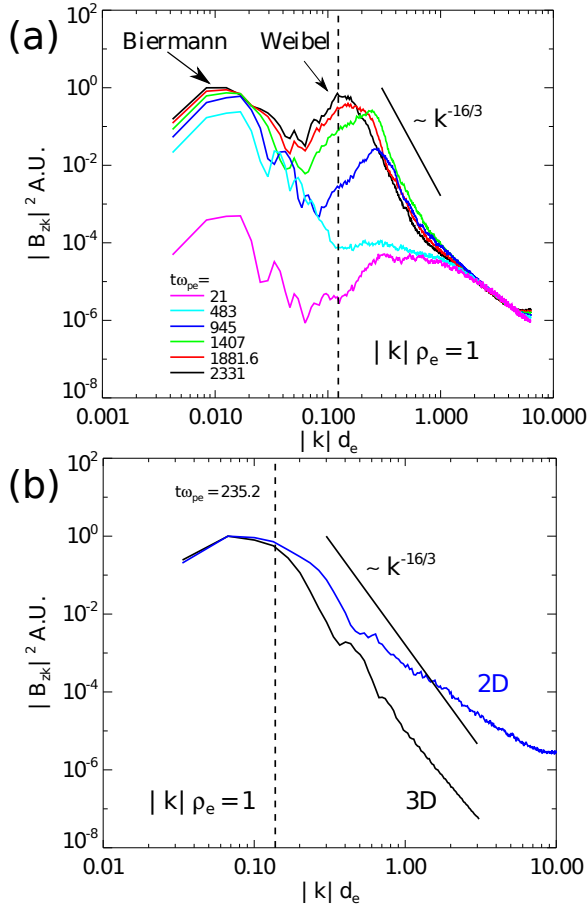


FIG. 5. Fourier spectrum of B_z^2 for (a) $L_T/d_e = 400$, and (b) $L_T/d_e = 50$. In (a) the spectrum is shown at several different times (see Fig. 3(a)) while in (b) the 3D (black curve) and the 2D simulation (blue curve) are shown for $t\omega_{pe} = 235.2$. The dashed lines represent where $k\rho_e = 1$, based on the maximum magnetic field. The solid black lines indicate a power law of $k^{-16/3}$.

deed to be expected for Biermann generated fields; also, at these small scales the electrons are not coupled to the ions, and are thus free to move at their thermal velocity. A transition to a logarithmic dependence on the system size occurs after $L_T/d_e > 50$; this is expected since the Weibel instability amplifies the magnetic fields at an exponential rate.

Spectra. Fig. 5(a) shows the spectrum of B_z^2 for our largest simulation ($L_T/d_e = 400$) at the times indicated in the inset of Fig. 3(a). At early times a peak rapidly forms at $kd_e \approx 0.01$, which corresponds to the large scale Biermann-generated magnetic field. At later times, a second peak corresponding to the Weibel generated magnetic fields begins to form at $kd_e \approx 0.2$ and eventually saturates at $kd_e \approx 0.1$; this scale exactly corresponds to $k\rho_e = 1$, where ρ_e is the electron Larmor radius based on the maximum B_z at saturation. Therefore, the Weibel generated fields saturate when $\beta_e = (\rho_e/d_e)^2 \approx 100$ (cf. [15]), in quantitative agreement with Fig. 3(b), and

independent of the system size.

Another remarkable feature yielded by the spectra of Fig. 5 is the power law behavior of the magnetic energy at sub- ρ_e scales, with a slope close to $-16/3$. A less steep power law appears to exist at smaller scales, but this is not present in the 3D simulation, where the $\sim k^{-16/3}$ behavior persists down to the smallest scales in the simulation, as seen in Fig. 5(b). Such a power law dependence was theoretically predicted in [18], where it was identified as resulting from the collisionless damping of kinetic Alfvén waves at $k\rho_e \sim 1$. To the best of our knowledge, this is the first 3D confirmation of that prediction, although similar observations have been made in 2D simulations [19].

Conclusions. We have performed fully kinetic simulations of magnetic field generation and amplification in expanding plasmas with perpendicular density and temperature gradients. For relatively small systems, $L_T/d_e < 100$, we observe the production of large-scale magnetic fields via the Biermann battery effect, fully confirming the theoretical predictions of Haines [7], in particular the scaling of the magnetic field strength with d_i/L_T . For larger systems, however, we discover a new regime of magnetic field generation: the expanding plasmas are Weibel unstable, giving rise to small scale ($\sim 5d_e$) magnetic fields whose saturated amplitude is such that $\beta_e \approx 100$, independent of system size, and thus much larger than would be predicted for such systems on the basis of the Biermann mechanism.

Unlike the Biermann effect, where magnetic fields arise in the absence of a seed, Weibel generated fields require an initial seed. In our simulations, this seed can either be due to low amplitude numerical noise, or to the Biermann generated fields. In real systems, however, we conjecture that the Biermann effect generates the magnetic fields that will then be amplified by the Weibel instability. We stress that while Biermann fields grow linearly in time, those due to Weibel grow exponentially.

These findings may significantly impact the canonical picture of cosmic magnetic field generation [1], by suggesting that Biermann seed fields may be pre-amplified exponentially fast via the Weibel instability up to reasonably large values (i.e., independent of the system size) previous to turbulent dynamo action.

In addition, a reinterpretation of some laser-solid experiments where magnetic field generation is observed may be in order. In two experiments at the OMEGA EP laser facility [10, 11], for example, where $L_T/d_i \approx 100$, our results suggest that the magnetic fields are generated in the Weibel regime, while an experiment at the Rutherford Appleton Laboratory [9] operates in the Biermann dominated regime, $L_T/d_i \approx 1$. In [9, 10] the measured values of β are $\beta < 100$, consistent with our predictions (note that in the absence of the Weibel instability, the predicted β for Ref. [10] on the basis of the Biermann mechanism would be $\beta \approx 10^4$). Due to the lack of a

reliable measurement of magnetic field, β was not calculated in [11]. However, proton imaging techniques are consistent with magnetic fields of order 0.1 megagauss [11]. Magnetic fields this large are indeed suggested by our results, with $\beta \sim 100$. Although we have not explored the mass ratio dependence of our results, this agreement between experiments and our simulations suggests that it should not significantly affect our main conclusions.

Acknowledgments. This work was partially supported by Fundação para a Ciência e Tecnologia (Ciência 2008 and Grant nos. PTDC/FIS/118187/2010 and PTDC/FIS/112392/2009), by the European Research Council (ERC-2010-AdG Grant no. 267841), and by the European Communities under the Contract of Association between EURATOM and IST. Simulations were carried out at Kraken, NICS (XSEDE Grant AST030030).

-
- [1] R. M. Kulsrud and E. G. Zweibel, Rep. Prog. Phys. **71**, 046901 (2008).
 - [2] R. M. Kulsrud and S. W. Anderson, Astrophys. J. **396**, 606 (1992).
 - [3] A. Brandenburg, D. Sokoloff, and K. Subramanian, Space Sci. Rev. **169**, 123 (2012).
 - [4] L. Biermann, Z. Naturforsch. **5a**, 65 (1950).
 - [5] C. E. Max, W. M. Manheimer, and J. J. Thomson, Phys. Fluids **21**, 128 (1978).
 - [6] R. S. Craxton and M. G. Haines, Plasma Phys. **20**, 487 (1978).
 - [7] M. G. Haines, Phys. Rev. Lett. **78**, 254 (1997).
 - [8] J. A. Stamper, K. Papadopoulos, R. N. Sudan, S. O. Dean, and E. A. McLean, Phys. Rev. Lett. **26**, 1012 (1971).
 - [9] P. M. Nilson, L. Willingale, M. C. Kaluza, C. Kamperidis, S. Minardi, M. S. Wei, P. Fernandes, M. Notley, S. Bandyopadhyay, M. Sherlock, R. J. Kingham, M. Tatarakis, Z. Najmudin, W. Rozmus, *et al.*, Phys. Rev. Lett. **97**, 255001 (2006).
 - [10] C. K. Li, F. H. Seguin, J. A. Frenje, J. R. Rygg, R. D. Petrasso, R. P. J. Town, O. L. Landen, J. P. Knauer, and V. A. Smalyuk, Phys. Rev. Lett. **99**, 055001 (2007).
 - [11] N. L. Kugland, D. D. Ryutov, P.-Y. Chang, R. P. Drake, G. Fiksel, D. H. Froula, S. H. Glenzer, G. Gregori, M. Grosskopf, M. Koenig, Y. Kuramitsu, C. Kuranz, M. C. Levy, E. Liang, *et al.*, Nature Phys. **8**, 809 (2012).
 - [12] E. S. Weibel, Phys. Rev. **114**, 18 (1959).
 - [13] R. A. Fonseca, L. O. Silva, F. S. Tsung, V. K. Decyk, W. Lu, C. Ren, W. B. Mori, S. Deng, S. Lee, T. Katsouleas, and J. C. Adam, Lect. Notes Comp. Sci. **2331**, 342 (2002).
 - [14] R. A. Fonseca, S. F. Martins, L. O. Silva, J. W. Tonge, F. S. Tsung, and W. B. Mori, Plasma Phys. Control. Fusion **50**, 124034 (2008).
 - [15] F. Califano, F. Pegoraro, S. V. Bulanov, and A. Mangeney, Phys. Rev. E **57**, 7048 (1998).
 - [16] R. A. Fonseca, L. O. Silva, J. W. Tonge, W. B. Mori, and J. M. Dawson, Phys. Plasmas **10**, 1979 (2003).
 - [17] K. Molvig, Phys. Rev. Lett. **35**, 1504 (1975).
 - [18] A. A. Schekochihin, S. C. Cowley, W. Dorland, G. W. Hammett, G. G. Howes, E. Quataert, and T. Tatsuno, Astrophys. J. Suppl. Ser. **182**, 310 (2009).
 - [19] E. Camporeale and D. Burgess, Astrophys. J. **730**, 8 (2011).